

## 3D level set modeling of static recrystallization considering stored energy fields



Benjamin Scholtes<sup>a,b,\*</sup>, Romain Boulais-Sinou<sup>a</sup>, Amico Settefrati<sup>b</sup>, Daniel Pino Muñoz<sup>a</sup>,  
Isabelle Poitraul<sup>c</sup>, Aurore Montouchet<sup>d</sup>, Nathalie Bozzolo<sup>a</sup>, Marc Bernacki<sup>a</sup>

<sup>a</sup> Mines-ParisTech, PSL-Research University, CEMEF – Centre de mise en forme des matériaux, CNRS UMR 7635, CS 10207, rue Claude Daunesse, 06904 Sophia Antipolis Cedex, France

<sup>b</sup> Transvalor S.A., 694, avenue Maurice Donat, 06250 Mougins, France

<sup>c</sup> Industeel, ArcelorMittal, CRMC, 71200 Le Creusot, France

<sup>d</sup> Areva Creusot Forge, 6 allée J. Perrin, 71200 Le Creusot, France

### ARTICLE INFO

#### Article history:

Received 1 February 2016

Received in revised form 19 April 2016

Accepted 28 April 2016

#### Keywords:

Full field modeling

Level-set

Static recrystallization

### ABSTRACT

In the last decades, many numerical models have been proposed to simulate thermomechanical treatments and their related effects on the microstructure. The present study deals with a relatively recent full field model using the level set method within a finite element framework. The ability of this approach to consider static recrystallization in two and three dimensions with nucleation has been demonstrated in previous studies (Bernacki et al., 2008, 2009). Although accurate, this model lies on a numerical formalism which is rather inefficient from a numerical point of view and do not permit to consider complex 3D aggregates in reasonable computation times. The present paper introduces a new efficient implementation of the static recrystallization (SRX) model which aims to overcome this limitation by taking full advantage of recent numerical developments (Shakoor et al., 2015; Scholtes et al., 2015). Its efficiency is evaluated through large scale 3D simulations of SRX with several thousand of grains. Acceleration factors of up to 40 are obtained, compared with the existing implementation. The predictions in terms of evolution of the recrystallized fraction are also confronted with classical analytic models and experimental results from literature, showing good agreement.

© 2016 Elsevier B.V. All rights reserved.

### 1. Introduction

The mechanical and thermal properties of metallic materials are strongly related to their microstructure. The understanding and the modeling of the microstructural evolution mechanisms is then crucial when it comes to optimize the forming process and the final in-use properties of the materials. During deformation, a portion of the energy remains stored in the material under the form of metallurgical defects (mostly dislocations), leaving the material in an unstable state from a thermodynamic point of view. Depending on the amount of stored energy, different phenomena can then become active in order to recover equilibrium (recrystallization, grain growth, recovery...). The understanding and modeling of these phenomena is a complex topic of great interest in the literature. Among all, recrystallization (ReX) corresponds to the rearrangement of grain boundaries (*i.e.* the grain interfaces) under

the effect of stored energy gradients throughout the microstructure. This process can appear during the deformation stage (dynamic recrystallization, DRX). It can also continue during a thermal post-treatment (post-dynamic recrystallization, PDRX), or be only activated during this post-treatment (SRX).

Thanks to the explosion of the computer capacities, very precise numerical techniques are now available to model ReX. These lower scale approaches, the so-called *full field* models, are based on a complete description of the microstructure topology at the polycrystal scale. Over the last decades, several mesoscale numerical models have been proposed to simulate ReX [5,6]. Probabilistic voxel-based approaches such as Monte Carlo [7,8] (MC) and cellular automata [9,10] (CA) are very popular. Furthermore, these methods scale extremely well with parallelization as they rely on regular grids, but the lack of physical time in the MC method and the difficulty to approximate accurately the grain boundary curvature with CA are still open issues. There are also difficulties with these approaches to treat the polycrystal deformation and the grain boundary motion in the same numerical framework. There are also deterministic approaches, which are more precise, as they do not rely on probabilistic laws, but also more greedy in terms of

\* Corresponding author at: Mines-ParisTech, PSL-Research University, CEMEF – Centre de mise en forme des matériaux, CNRS UMR 7635, CS 10207, rue Claude Daunesse, 06904 Sophia Antipolis Cedex, France.

E-mail address: [benjamin.scholtes@mines-paristech.fr](mailto:benjamin.scholtes@mines-paristech.fr) (B. Scholtes).

computational resources due to the fact that they involve the resolution of large systems of partial differential equations (PDEs). Thus several workers have developed the vertex method [11,12], wherein the grain boundaries are defined in terms of vertices; the interface motion is then imposed by the displacement of a set of points. A limitation of these front-tracking approaches lies in the handling of topological events (grain shrinkage, appearance of a nucleus) in three dimensions. Another approach found in the literature uses the phase-field (PF) method, which offers the advantage of avoiding the difficult problem of tracking interfaces [13,14]. Finally, ReX can also be modeled using a level set (LS) description of the interfaces in a finite element (FE) framework [15,16,17] or in the context of uniform grids with Fourier transform resolution [18]. The FE–LS and FE–PF methods are actually quite close and share some common features (no explicit tracking of the interfaces, deterministic approach lying on the solving of PDE systems). Although the PF method lies on strong physical and thermodynamical foundations, its formulation introduces purely numerical parameters (like the grain boundary width). On the other hand, the LS method only requires measurable quantities which have a direct physical interpretation, making it a priori more simple to use [19]. One interest of using a FE framework instead of uniform grids is the possibility to handle large polycrystal deformations with the well-known Crystal Plasticity Finite Element Method (CPFEM) [16,2,15] and to deal with a global resolution framework concerning the modeling of the thermomechanical treatments and their subsequent microstructure evolutions.

The full field modeling of ReX using unstructured FE meshes is a very exciting research topic due to the possibility to simulate many physical phenomena (particle pinning, annealing twin development, solute drag, CPFEM and field dislocation mechanics...). However, the numerical cost of these approaches remains their main drawback, explaining why they are hardly used in 3D. Recently, new numerical tools have been proposed to increase the numerical efficiency of these models, which are respectively a direct and parallel reinitialization method [3] and an efficient recoloring scheme enabling to perform optimized and coalescence-free simulations [4]. These optimizations have been tested in the context of pure grain growth (GG) in two and three dimensions, and have permitted significant time and memory savings. Nevertheless the ReX formalism employed in [1] is not compatible with the recoloring scheme introduced in [4]. It is also extremely greedy in terms of computational resources. The present paper thus aims to introduce an optimized implementation of the ReX model enabling to perform 3D simulations of SRX with reasonable computational efforts.

After recalling the main features of the present FE–LS numerical model in the next section, the new ReX formalism and its implementation are extensively detailed in the third section. The efficiency of the new model is finally challenged in the last section through realistic 3D SRX simulations and the numerical predictions in terms of recrystallized fraction are confronted with classical analytic laws and experimental observations from the literature. It is especially demonstrated that the improved model is very efficient from a numerical aspect and captures well the recrystallization kinetics.

## 2. Initial formalism and limitations

As mentioned above, the model considered in this paper uses a LS description of the interfaces in a FE framework. A LS function  $\psi$  is defined over a domain  $\Omega$  as the signed distance function to the interface  $\Gamma$  of a sub-domain  $G$  of  $\Omega$ . The values of  $\psi$  are calculated at each interpolation point (node in the considered P1 formulation) and the sign convention states  $\psi \geq 0$  inside  $G$  and  $\psi \leq 0$  outside:

$$\forall t \begin{cases} \psi(x, t) = \pm d(x, \Gamma(t)), & x \in \Omega, \\ \Gamma(t) = \{x \in \Omega, \psi(x, t) = 0\}, \end{cases} \quad (1)$$

where  $d(x, \Gamma(t))$  corresponds to the Euclidean distance between a point  $x \in \Omega$  and the interface  $\Gamma$  of the sub-domain  $G$ .

The LS interface is then displaced according to a given velocity field  $\vec{v}$  by solving a transport equation:

$$\begin{cases} \frac{\partial \psi(x, t)}{\partial t} + \vec{v} \cdot \nabla \psi(x, t) = 0, \\ \psi(x, t = 0) = \psi^0(x), \end{cases} \quad (2)$$

It is well admitted that the velocity of a grain boundary  $\vec{v}$  can be expressed as the sum of two terms:

$$\vec{v} = \vec{v}_{gg} + \vec{v}_e, \quad (3)$$

with  $\vec{v}_{gg}$  and  $\vec{v}_e$  the capillarity and stored energy contributions, respectively (see Fig. 1).

In a level set (LS) framework, the former can be expressed as follows [20,17]:

$$\vec{v}_{gg} = -m\gamma\Delta\psi\nabla\psi, \quad (4)$$

by assuming that the LS function  $\psi$  is nearly a distance function (*i.e.*  $\|\nabla\psi\| = 1$ ) at least inside a thin layer  $\pm\varepsilon$  around the interface. In this expression,  $M$  and  $\gamma$  are respectively the grain boundary mobility and energy. For the sake of simplicity, the terms  $N_g$  and  $N_p$  are introduced in order to designate, respectively, the number of grains and the number of LS functions used to represent the microstructure. A simple option consists in representing each grain by a LS function, which leads to  $N_p = N_g$ . An alternative is the use of a *coloring* technique, which enables to limit the number of needed functions  $N_p < N_g$ . See [4] for further details. Given the previous simplifications, the transport problem of Eq. (2) can be easily reformulated as a set of  $N_p$  convective–diffusive equations (CDEs):

$$\begin{cases} \frac{\partial \psi_i(x, t)}{\partial t} - M\gamma\Delta\psi_i(x, t) + \vec{v}_e \cdot \nabla \psi_i(x, t) = 0, & \forall i \in \{1, \dots, N_p\}, \\ \psi_i(x, t = 0) = \psi_i^0(x), \end{cases} \quad (5)$$

associated with the condition  $\|\nabla\psi_i(x, t)\| = 1, \forall i \in \{1, \dots, N_p\}, \forall x/|\psi_i(x, t)| \leq \varepsilon$ .

On the other hand, the computation of the term  $\vec{v}_e$  requires more attention. This term actually depends on the stored energy gradients throughout the microstructure. In [1], the energy is assumed homogeneous inside a given grain, which implies that the energy gradient is non-zero only at grain boundaries and null elsewhere. In other words, intragranular heterogeneities are not

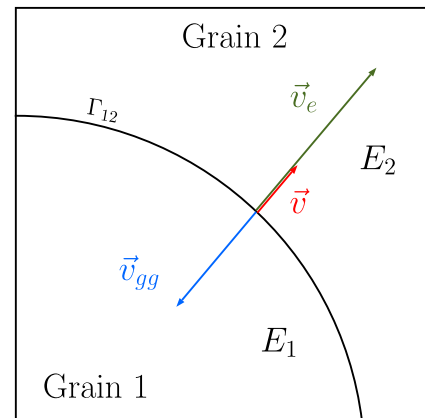


**Fig. 1.** Velocity  $\vec{v}$  of a grain boundary consisting of a capillarity contribution  $\vec{v}_{gg}$  and a term representing the energy jump across the interface  $\vec{v}_e$ . Here, the concave shape of  $\Gamma_{12}$  gives the orientation of  $\vec{v}_{gg}$  and it is assumed that  $E_1 < E_2$ , explaining why the vector  $\vec{v}_e$  is oriented from  $G_1$  toward  $G_2$ .

considered and energy is assumed spatially constant in a given grain. Furthermore, this formulation lies also on a constant energy values  $e_i$  for each LS functions  $\psi_i$ , which can be time-dependent, eventually. Given the previous statements, the most natural way to compute the term  $\bar{v}_e$  in the vicinity of a grain boundary separating the grains of indexes  $i$  and  $j$  is as follows [2]:

$$\bar{v}_e(x, t) = M_{ij} f(\psi_i(x, t), l) (e_j(t) - e_i(t)) \frac{\nabla \psi_i(x, t)}{\|\nabla \psi_i(x, t)\|}, \quad (6)$$

where  $f$  is a decreasing function varying from 1 (for  $\psi_i = 0$ ) to 0 (for  $\psi_i = l$ ), and  $M_{ij}$  is the interface mobility between grains  $i$  and  $j$ . Hereafter the grain boundary mobility is assumed homogeneous throughout the microstructure, with a constant  $M$  value. Furthermore, the time variable will now be systematically omitted for the sake of clarity, although it is obvious that all considered quantities are (or can be seen as) time-dependent.

Nevertheless this simple formulation generates discontinuities at multiple junctions which result in ill-conditioned problems. An alternative to avoid this issue was proposed in [1]. It uses the weighted contributions of all the LS functions and their respective energies at each node of the FE mesh:

$$\bar{v}_e(x) = M \sum_{i=1}^{N_p} \sum_{j=1}^{N_p} \chi_i(x) f(\psi_j(x), l) (e_j - e_i) \frac{\nabla \psi_j(x)}{\|\nabla \psi_j(x)\|}, \quad (7)$$

with  $\chi_i$  the characteristic function of the  $i^{\text{th}}$  LS function  $\forall i \in \{1, \dots, N_p\}$ . This formulation has the advantage of avoiding the identification of the neighboring grains and leads to a smooth velocity field even at multiple junctions.

This approach has been extensively tested and validated in [1,2]. However in these works, each grain is represented by a LS function (*i.e.*  $N_p = N_g$ ) in order to consider an independent energy level for each grain. This approach is therefore not compatible with large scale simulations, especially in 3D, because the numerical cost of these simulations depends strongly on the number of LS functions. For this reason, a coloring technique is used, whose principle is to represent a set of distinct grains by the same Global Level Set (GLS) function [21]. By this mean, the number of needed functions  $N_p$  can be considerably reduced  $N_p \ll N_g$  (Fig. 2). Nevertheless, there are incompatibilities between this coloring approach and the above ReX formalism [1]:

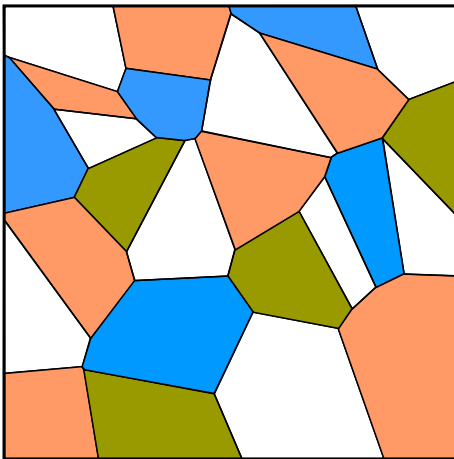


**Fig. 2.** 25 grains microstructure represented by four GLS functions, respectively colored in white, green, orange and blue. (For interpretation of the references to color in this figure legend, the reader is referred to the web version of this article.)

- given that the energy is a quantity which is constant for a given GLS function, all the grains represented by this function have necessarily the same energy, which makes no sense from a metallurgical point of view,
- each recoloring operation (see [4] for details) would inevitably modify the energy of the concerned grain, which would receive the energy corresponding to the recipient GLS function and lose the energy associated with its own mechanical state.

In the next section, a new implementation of the ReX model is proposed. Although it is much more numerically efficient and permits to take full advantage of the recoloring technique detailed in [4], this new implementation is strictly equivalent to the current one from a metallurgical point of view.

One major drawback of the LS approach lies in the possible alteration of the metric property during the transport stage (*i.e.*  $\|\nabla \psi\| \neq 1$ ). This is particularly problematic when a specific remeshing technique depending on the distance property is used at the interface. Furthermore the diffusive formulation introduced in Eq. (5) remains valid only if the function  $\psi$  is locally a distance function. Finally, the condition number associated with our weak formulation (P1 interpolation, implicit method) depends largely on the regularity of the function  $\psi$  [1].

The distance function must therefore be reinitialized at each time step to recover the metric property  $\|\nabla \psi\| = 1$ . This operation is performed through a parallel and direct reinitialization algorithm detailed in [3], which has been proven to be extremely fast and accurate. In this algorithm, the GLS interface is firstly discretized into a collection of segments (respectively triangles in 3D) and the nodal values of the GLS function are then updated by finding the nearest element of the collection and calculating the distance between the considered node and this nearest element. This method takes advantage of a space-partitioning technique using  $k$ -d tree and an efficient bounding box strategy enabling to maximize the numerical efficiency for parallel computations.

### 3. New implementation of the ReX formalism

The objective is to create a new description of the polycrystal wherein each grain has its own energy which is completely independent of the GLS functions. The probably most natural way to achieve this goal consists in replacing the energy  $e_i$  (constant for the whole FE mesh) of each GLS function by an energy field  $\mathcal{E}_i(x)$  evaluated at each interpolation point (see Fig. 3).

Such an extension is not straightforward and requires the developments of new algorithms to:

1. initialize the energy fields by assigning an energy level to each grain of the microstructure at an early stage of the simulation, with respect to a prescribed energy field,
2. compute the velocity field  $\bar{v}_e$  with an energy which is no more constant for a given GLS function,
3. track the respective grain energies during the simulation,
4. handle efficiently nucleation events in order to limit the number of GLS functions and maintain low computational costs.

It is worth emphasizing that, even if the present study deals only with scalar energy fields, the algorithms introduced in this section are completely general and address also problems involving vector and/or tensor fields. The interested reader may find an other example of application in [22], in which the same tools are employed to handle the crystal orientation fields in the context of DRX.

### 3.1. Initialization of the energy fields

The first step consists in initializing the energy fields  $\mathcal{E}_i(x)$ . This operation is performed in two stages:

1. the separation of the connected components (SCC) in order to identify the grains represented by the same GLS function,
2. the generation and assignation of the grain energies.

The SCC algorithm is extensively detailed in [4] and returns, for each GLS function  $\psi_i$ , an index field noted  $\mathcal{I}_i$ , wherein each grain is represented by a unique identifier (see Fig. 4).

Let us designate by  $G_i$  the number of grains represented by the  $i^{\text{th}}$  GLS function at a given time. After performing the SCC algorithm, an energy value is generated for each grain of index  $g \in \{1, \dots, G_i\}$ . These values can be directly imported from CPFEM calculations or experimental data. In both cases, this procedure is designated by the function GENERATE\_VALUE() in Algorithm 1. Once the energies have been defined, the mesh nodes are scanned and the procedure detailed in Algorithm 1 is performed.

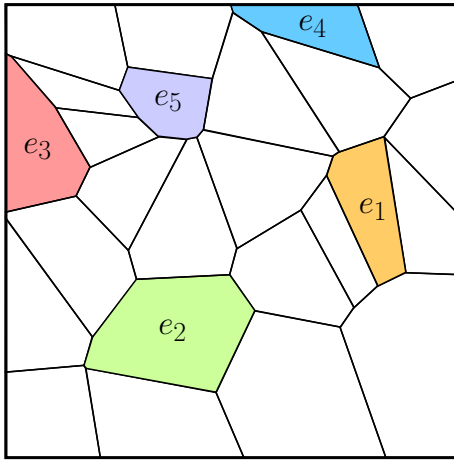


**Fig. 3.** An energy field  $\mathcal{E}_i(x)$  in which each grain has an independent energy. The blank zones correspond to an arbitrary negative value ( $-1$  for the sake of simplicity).

**Algorithm 1.** Initialization of the energy fields at the early stage of the simulation

---

```

procedure GENERATE_ENERGY Field  $\mathcal{I}_i$ 
  Create a Table  $E$  with size  $G_i$ 
  for Integer  $g \in \{1, \dots, G_i\}$  do
     $E[g] \leftarrow \text{GENERATE\_VALUE}()$ 
  end for
  for Node  $n \in \mathcal{M}$  do
    if  $\mathcal{I}_i(n) > 0$  then
       $\mathcal{E}_i(n) \leftarrow E[\mathcal{I}_i(n)]$ 
    else
       $\mathcal{E}_i(n) \leftarrow -1$ 
    end if
  end for
  return  $\mathcal{E}_i$ 
end procedure

```

---

When a node  $n$  satisfying  $\mathcal{I}_i(n) > 0$  is met, the corresponding energy field receives the value previously generated for this grain identifier. In the zones where  $\mathcal{I}_i = 0$ , the energy field  $\mathcal{E}_i$  is set to an arbitrary negative value ( $-1$  for simplicity), which indicates that it is an undefined region. Fig. 3 illustrates the result obtained by executing this procedure on the microstructure shown in Fig. 4(b).

### 3.2. Calculation of the velocity field $\vec{v}_e$

Considering that in our new formalism energy is no longer a constant but a space-dependent variable, it seems obvious to reformulate Eq. (7) as follows:

$$\vec{v}_e(x) = M \sum_{i=1}^{N_p} \sum_{j=1}^{N_p} \chi_i(x) f(\psi_j(x), l) (\mathcal{E}_i(x) - \mathcal{E}_j(x)) \frac{\nabla \psi_j(x)}{\|\nabla \psi_j(x)\|}. \quad (8)$$

However, this extension makes no sense if used as such because all the energy fields  $\mathcal{E}_j$  (with  $j \neq i$ ) are not defined inside the  $i^{\text{th}}$  GLS function (i.e. where  $\chi_i = 1$ ). Let us illustrate this situation with the simple two-grain microstructure depicted in Fig. 5(a). These grains are respectively represented by two GLS function,  $\psi_1$  and  $\psi_2$ , and two energy fields  $\mathcal{E}_1$  and  $\mathcal{E}_2$  (see Fig. 5(b) and (c)).

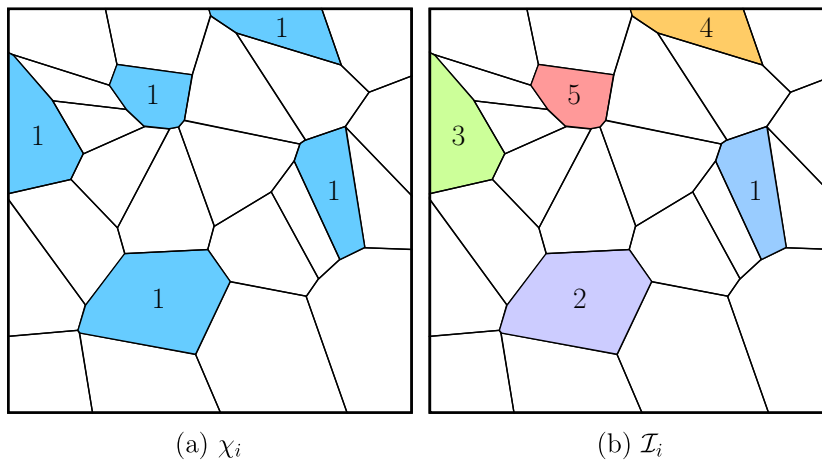


**Fig. 4.** Characteristic (a) and index (b) fields of a GLS function used to represent five grains. Unlabeled grains receive a null value.

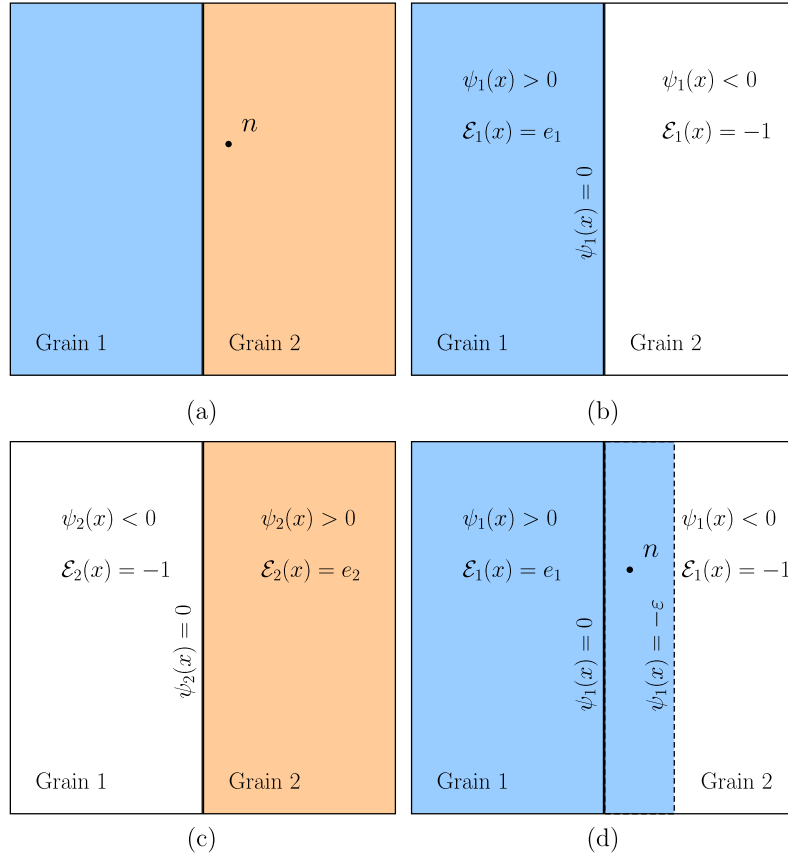


Fig. 5. Simple two-grain microstructure illustrating the problem of computing the  $\vec{v}_e$  velocity field with the new formulation of Eq. (8).

At the node  $n$  represented in Fig. 5(a),  $\chi_1$  is naturally equals to 0 and Eq. (8) boils down to:

$$\vec{v}_e(n) = Mf(\psi_1(n), l)(\mathcal{E}_2(n) - \mathcal{E}_1(n)) \frac{\nabla\psi_1(n)}{\|\nabla\psi_1(n)\|}. \quad (9)$$

Nevertheless the value of  $\mathcal{E}_1$  at this node is negative, because it is located in the undefined region of the field.

To solve this issue, the energy fields must be extended outwards their respective GLS functions before computing the velocity field  $\vec{v}_e$ . While  $G_i > 1$ , the nodal value of a GLS function corresponds to the distance of the nearest grain it contains. The energy fields must therefore be extended in  $\psi_i \in [-\epsilon, 0]$  with the energy value of this nearest grain. This operation should therefore be performed simultaneously with reinitialization in order to keep high numerical efficiency.

The direct reinitialization algorithm introduced in [3] computes, for each node, the distance to the nearest facet (segment in 2D, triangle in 3D) constituting the piece-wise linear contour. As it is insufficient in our case, it has been implemented in a different manner. Thus, the new implementation now returns directly the nearest element with all its associated features (coordinates of the delimiting points, normal vector, field values...). Considering that the only quantity of interest in the context of SRX is the stored energy, a unique scalar value is attached to each facet during the construction of the discretized interface. This value corresponds obviously to the energy of the grain surrounded by this facet. During the reinitialization stage, the energy attached to the nearest element is used to complete the stored energy field in  $\psi_i \in [-\epsilon, 0]$  (see Fig. 6(a)). A great advantage of this new implementation lies also on the possibility to compute the exact gradient of the GLS function  $\nabla\psi$ , by projecting the reinitialized node on the nearest

facet (see Fig. 6(b)). The nodal value of  $\nabla\psi$  is finally used in Eq. (8) to compute the velocity field  $\vec{v}_e$ .

The reinitialization of the distance functions and the extension of the energy fields are thus performed simultaneously, which involves few additional computations compared to a classical reinitialization (without field extension). The impact of the field extension procedure on the computation time is discussed in the fourth section. Going back to the previous two-grain microstructure, the result of the reinitialization/extension procedure performed on the energy field  $\mathcal{E}_1$  is depicted in Fig. 5(d). The energy field now lives also in  $[-\epsilon, 0]$ , which allows a correct computation of the velocity field  $\vec{v}_e$  at the node  $n$ , through Eq. (9).

### 3.3. Tracking of the grain energies

After the velocity field  $\vec{v}_e$  has been computed, the GLS functions  $\psi_i$  evolve accordingly to the system of CDEs defined by Eq. (5).

For convenience, we introduce the notation  $\mathcal{N}_{g,i}$  to represent the set of nodes located inside the grain with index  $g \in \{1, \dots, G_i\}$ , represented by the function  $\psi_i$ . Hereafter the superscripts  $\cdot^t$  and  $\cdot^{t+\Delta t}$  are employed to designate the values of a field before and after the solving of the CDEs, respectively.

The energy fields  $\mathcal{E}_i$  must be updated at each time step to ensure the energies remain fitted on their respective grains between two consecutive increments. The employed procedure is relatively simple and consists in two steps:

- for each grain of index  $g \in \{1, \dots, G_i\}$ , search the maximal positive energy value of the field  $\mathcal{E}_i^t$  in the set of nodes  $\mathcal{N}_{g,i}^{t+\Delta t}$ ,
- perform a second loop and assign this maximal energy to the field  $\mathcal{E}_i^{t+\Delta t}$  in all the nodes belonging to  $\mathcal{N}_{g,i}^{t+\Delta t}$ ,

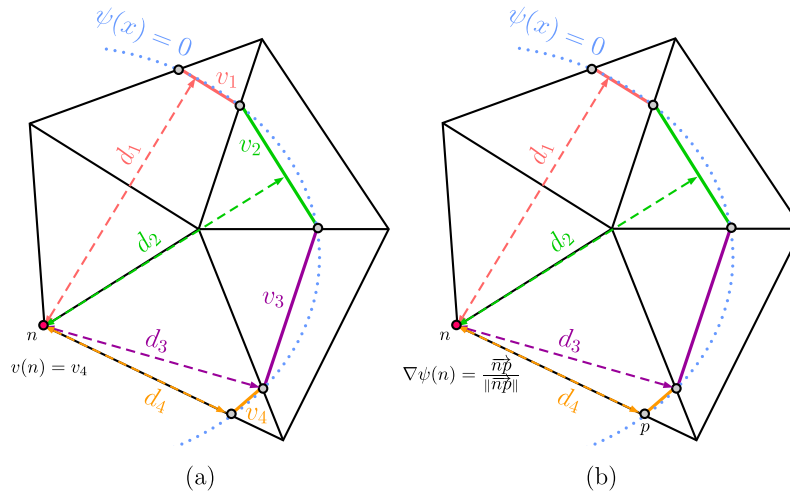


Fig. 6. Field extension (a) and computation of the exact gradient  $\nabla\psi$  (b) with the reinitialization algorithm.

- all other nodes  $n \notin \mathcal{N}_{g,i}^{t+\Delta t}$  are tagged with  $-1$  (undefined region).

It is obvious such an algorithm requires the existence of an overlap area between the old and updated positions of each grain, i.e.:

$$\mathcal{N}_{g,i}^t \cap \mathcal{N}_{g,i}^{t+\Delta t} \neq \emptyset, \quad (10)$$

in order to perform the identification. In other words, at least one node having a positive energy value must be found in  $\mathcal{N}_{g,i}^{t+\Delta t}$ . In practice, Eq. (10) is not satisfied in the two following configurations:

- $\mathcal{N}_{g,i}^{t+\Delta t} = \emptyset$ , i.e. when the grain of index  $g$  disappears,
- $\mathcal{N}_{g,i}^{t+\Delta t} \neq \emptyset$  but the displacement of  $g$  during  $t$  and  $t + \Delta t$  is so important that  $\mathcal{N}_{g,i}^t \cap \mathcal{N}_{g,i}^{t+\Delta t} = \emptyset$ ,

Case (a) is actually not problematic as the energy of a dying grain must necessarily be removed from the energy field, which is what it is done by the algorithm. On the other hand, the scenario (b) must absolutely be avoided. If it occurs, the considered grain would lose its energy and receive a negative value instead, as illustrated in Fig. 7. To prevent this issue, it appears crucial to ensure a

proper identification of all the grains between two consecutive increments. The satisfaction of this condition is actually strongly related to the time step  $\Delta t$ . As a simple example, let us consider a grain and the sphere centered on its centroid, which have a sufficient radius  $R_{eq}$  to contain this grain. In this configuration, it is obvious that Eq. (10) is verified between two consecutive increments as long as:

$$\Delta t < \frac{R_{eq}}{v_{max}}, \quad (11)$$

where  $v_{max}$  is the maximal velocity magnitude at the interface of the considered grain. A worst case scenario for the satisfaction of this inequality comes when a shrinking grain becomes very close of the mesh size  $R_{eq} \sim h$ . However, given the typical values of  $v_{max}$  and  $h$  used in our simulations, the condition  $\Delta t < h/v_{max}$  is always easily verified, even with the large time steps allowed by our implicit numerical scheme. Fig. 7 illustrates the updating of an energy field. In this example, the grain with energy  $e_4$  disappears during the resolution of the CDEs. The grain having the energy  $e_5$  illustrates what happens when Eq. (10) is not satisfied, even if it has been demonstrated above that this scenario does not occur in practice.

The global algorithm for the updating of the energy fields is provided in Algorithm 2.

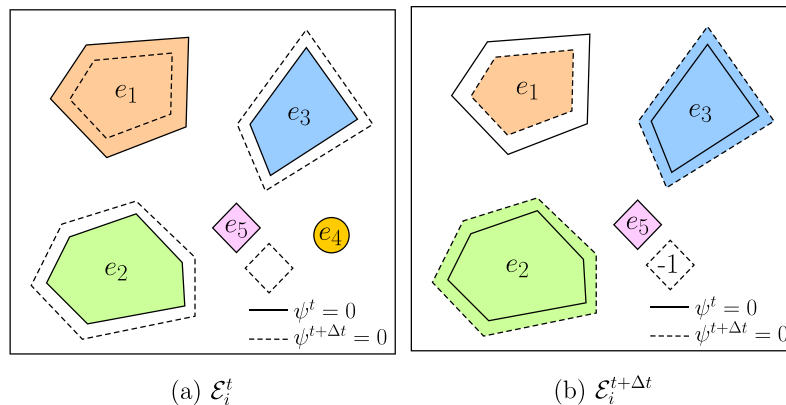


Fig. 7. Energy field  $\mathcal{E}_i^t$  before (a) and after (b) the updating procedure. The grain with energy  $e_4$  disappears between  $t$  and  $t + \Delta t$ . The white zone corresponds to an arbitrary negative value.

**Algorithm 2.** Updating of the energy fields between two consecutive increments

---

```

procedure UPDATE_ENERGY Field  $\mathcal{I}_i$ , Field  $\mathcal{E}_i^t$ 
  Create a Table  $E$  with size  $G_i$  and initialize its components
   $E[\cdot] \leftarrow -1$ 
  for Node  $n \in \mathcal{M}$  do
    if  $\mathcal{I}_i(n) > 0$  then
       $E[\mathcal{I}_i(n)] \leftarrow \max(E[\mathcal{I}_i(n)], \mathcal{E}_i^t(n))$ 
    end if
  end for
  Process synchronization  $\rightarrow$  keep the maximal value in  $E$ 
  component by component
  for Node  $n \in \mathcal{M}$  do
    if  $\mathcal{I}_i(n) > 0$  then
       $\mathcal{E}_i^{t+\Delta t}(n) \leftarrow E[\mathcal{I}_i(n)]$ 
    else
       $\mathcal{E}_i^{t+\Delta t}(n) \leftarrow -1$  (or any arbitrary negative value)
    end if
  end for
  return  $\mathcal{E}_i^{t+\Delta t}$ 
end procedure

```

---

### 3.4. Improvement of the nucleation algorithm

During annealing at elevated temperatures, a deformed microstructure usually recrystallizes discontinuously, through the appearance and growth of new grains with low dislocation density, the *nuclei*. This process is known as *discontinuous recrystallization*. On the other hand, the microstructure may also evolve relatively homogeneously throughout the material, with no recognizable ‘nucleation’ and ‘growth’ of the recrystallized grains. In these conditions, the process can reasonably be classified as *continuous recrystallization*. The microstructural mechanisms involved during discontinuous and continuous recrystallization are actually similar and the difference between these terminologies is purely phenomenological, referring only to the spatial and temporal heterogeneity of microstructural evolution [23].

In this section, we present an algorithm which enables to introduce dynamically new grains having their own features (stored energy, crystal orientation...) into the microstructure. Although only SRX in site saturated condition is considered in the present study, it is obvious that this algorithm can also be employed to address continuous ReX at the sub-grain scale.

During SRX, DRX or PDRX, nuclei can appear continuously during the treatment or in site-saturated conditions. When a nucleus emerges in the microstructure, it can grow or shrink, depending on the capillarity force, the local energy gradient and the mobility of the surrounding grain boundaries. In the present study, a constant mobility is assumed for all grain boundaries, which means that the behavior of a nucleus is only dictated by the balance between capillarity effects and stored energy gradients. In a LS framework, introducing new grains in the microstructure is straightforward because it relies on simple arithmetic operations on the distance functions. In [1,15], several SRX simulations have been performed in two and three dimensions. Nevertheless, these works are based on the initial ReX formalism detailed in Section 2, and then suffer from the above mentioned drawbacks. More specifically, in these simulations each grain and nucleus is represented by its own distance function, making this approach hardly compatible with large scale computations in 3D.

Next, we are interested in the improvement of this nucleation algorithm in order to take full advantage of the GLS functions

(reduction of the number of operations, dynamic recoloring, memory savings...). For the sake of simplicity, each nucleus is assumed perfectly circular. A set  $\mathcal{P}$  of all the potential nucleation sites is firstly constructed. It can contain all the nodes of the mesh or just a subset of them (e.g. nodes located inside a layer around the grain boundaries). A nucleation site with coordinates  $\mathbf{x}_g$  is then chosen in  $\mathcal{P}$ , randomly or with an eventual selection criterion (highest stored energy, closest point from the grain boundaries...). By noting  $r$  the initial radius of the germ, its distance function  $\phi$  can be simply calculated as follows:

$$\phi(\mathbf{x}) = r - \|\mathbf{x}_g - \mathbf{x}\|, \quad (12)$$

Next the new grain is affected to a GLS function. The index  $k$  is used hereafter to designate the GLS function which receives the nucleus. To determine  $k$ , we firstly evaluate, for each GLS function  $i$ , the minimal distance  $\Omega_i$  between this nucleus and the grains already represented by  $\psi_i$ . The  $k^{\text{th}}$  GLS function satisfying:

$$\Omega_k = \max_{\forall i \in \{1, \dots, N_i\}} (\Omega_i), \quad (13)$$

is finally chosen to host the germ, provided that  $\Omega_k \geq s$ , with  $s$  a positive security distance. If  $\Omega_k < s$ , no existing GLS function can receive the nuclei. A new function is therefore created  $N_p \leftarrow N_p + 1$  and initialized such as  $\psi_{N_p} = \phi$ .

All the nodes  $n$  satisfying  $\phi > 0$  are finally removed from  $\mathcal{P}$  to prevent the appearance of an other germ in the recrystallized region and the following arithmetic operations are performed on the GLS and stored energy fields:

$$\begin{aligned} \tilde{\psi}_i(\mathbf{x}) &= \begin{cases} \max(\psi_i(\mathbf{x}), \phi(\mathbf{x})) & \text{if } i = k \\ \min(\psi_i(\mathbf{x}), -\phi(\mathbf{x})) & \text{if } i \neq k \end{cases} \quad \text{and} \\ \tilde{\mathcal{E}}_i(\mathbf{x}) &= \begin{cases} e_0 & \text{if } i = k \\ -1 & \text{if } i \neq k \end{cases} \quad \forall i \in \{1, \dots, N_p\}, \end{aligned} \quad (14)$$

with  $e_0$  the stored energy level in the recrystallized material.

This procedure is repeated until the desired number of created nuclei is achieved or until the set  $\mathcal{P}$  becomes empty (which corresponds to a fully recrystallized microstructure).

### 3.5. Optimization of the recoloring scheme

In [4], a recoloring scheme working directly on unstructured FE meshes is detailed. This algorithm automatically detects the risk of numerical coalescence (i.e. fusion of grains belonging to the same GLS function) and perform preventive swapping (i.e. recoloring) operations to avoid this issue. The criterion which triggers the swapping operations in this previous work is the direct proximity in terms of neighborhood between the grains. More specifically, it is assumed that there exists a risk of coalescence whether two grains belonging to the same GLS function are separated by only one exterior grain. This swapping criterion is referred as  $C_1$  and presents the advantage of not introducing any numerical parameter. On the other hand, it may also be rather limiting when it comes to model particular microstructures, with strong size heterogeneities. Let us consider the polycrystal of Fig. 8(a) with dimensions  $0.3 \times 0.3 \times 0.3 \text{ mm}^3$ , composed of 48 grains and represented by  $N_p = 15$  colors.

300 nuclei are then introduced at the grain boundaries following the procedure detailed in Section 3.4, giving  $N_g = 348$ . Here the set  $\mathcal{P}$  is initialized with the nodes satisfying  $\max(\psi_p) \leq h$  in order to restrict nucleation in a narrow band around the gains boundaries. The minimal security distance  $s$  between the existing grains and the new germ is taken equals to the nuclei diameter  $2r$  (see Section 3.4 for explanations).

It is obvious such a microstructure presents strong grain size heterogeneities. More precisely, the larger grains act like bounds

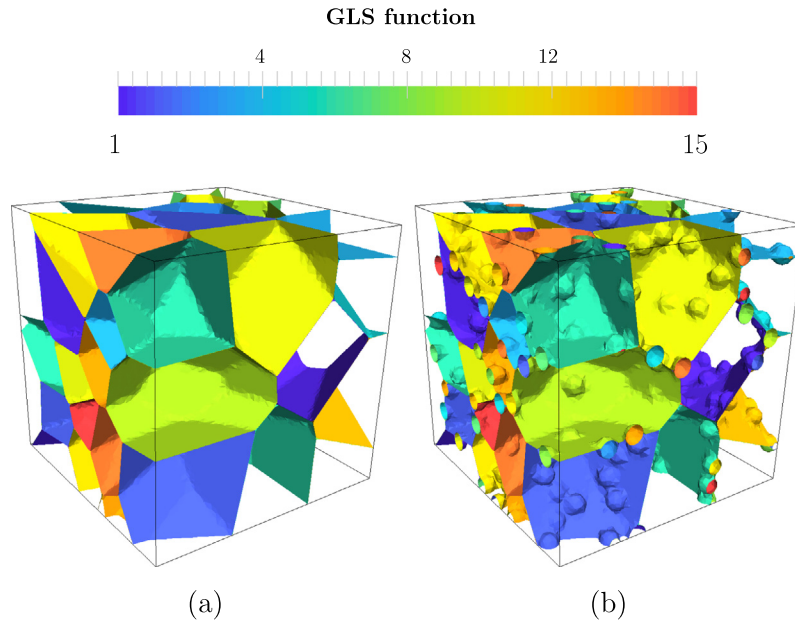


Fig. 8. (a) 3D polycrystal composed of 48 grains and represented by 15 GLS functions; (b) the same microstructure after nucleation at grain boundaries ( $N_g = 348, N_p = 15$ ).

between the nuclei, creating a large number of conflicts if the criterion  $C_1$  is used for the swapping procedure. By executing this version of the algorithm (as it is done in [4]) on the microstructure of Fig. 8(b), 69 new GLS functions are initialized to solve the conflicts, leading to  $N_p = 84$ , which is critically high. This situation is obviously problematic from a numerical point of view because the number of needed GLS functions determines the computation time. A new swapping criterion which can be seen as an extension of  $C_1$  has thus been developed. It is referred as  $C_2$  hereafter.

Let us designate by  $\mathcal{L}(g)$  the long range neighborhood of the grain with index  $g$ . Considering the  $C_1$  criterion,  $\mathcal{L}(g)$  contains all the first and second neighbors (FSN) of the grain  $g$ . More precisely, the term second neighbor of  $g$  is used to designate a grain which is a neighbor of at least one  $g$ 's neighbor, without being  $g$  itself. We also introduce the table  $\mathcal{C}(g)$  which returns the index  $p$  of the GLS function  $\psi_p$  that contains the grain of index  $g$ . Note  $g^*$  a second neighbor of  $g$ . With the  $C_1$  criterion,  $g^*$  is directly added in  $\mathcal{L}(g)$ , without any restriction. As a result, this table  $\mathcal{L}(g)$  finally contains all the first and second neighbors (FSN) of  $g$ . In practice, if the distance separating two grains remains sufficiently high, there is no risk of coalescence between two consecutive increments, even if they are separated by only one exterior grain. So, in the  $C_2$  procedure, the distance  $d(g, g^*)$  separating  $g$  and  $g^*$  is firstly evaluated in order to determine whether  $g^*$  is added in  $\mathcal{L}(g)$  or not. If  $d(g, g^*) > \xi$  (with  $\xi$  a simulation parameter), the second neighbor  $g^*$  is ignored, which has two consequences:

- no conflict can arise between  $g$  and  $g^*$ , even if  $\mathcal{C}(g) = \mathcal{C}(g^*)$ ,
- by assuming  $\mathcal{C}(g) \neq \mathcal{C}(g^*)$  initially, it is perfectly possible that they become represented by the same GLS function after the swapping procedure.

Thus it is obvious that working with  $C_1$  is equivalent to use  $C_2$  with  $\xi = \infty$ . In order to keep a high numerical efficiency, we do not compute the exact distance between  $g$  and  $g^*$  but the distance between their respective bounding boxes in the cartesian coordinate system used to generate the RVE. This distance determines whether  $g^*$  is accepted in  $\mathcal{L}(g)$  or not. The Fig. 9 illustrates these two situations: in Fig. 9(a), it is assumed that  $d(g, g^*) < \xi$ , which

implies  $g^*$  is added in  $\mathcal{L}(g)$ ; in Fig. 9(b), the grain  $g^*$  is ignored because the separation is sufficient.

By applying the above  $C_2$  procedure on the microstructure of Fig. 8(b) with  $\xi = \langle R \rangle_{\text{ReX}}$  (with  $\langle R \rangle_{\text{ReX}}$  being the mean recrystallized grain size), all the initial coloring conflicts can be solve without creating any new GLS functions, as illustrated in Fig. 8(b). Next, a heat treatment of 5 min at 1000 °C is simulated. A null stored energy is affected to the nuclei while the deformed grains present in Fig. 8(a) receive a value of  $3.3 \times 10^{-4}$  J/mm<sup>3</sup>, which is a realistic order of magnitude. The material and simulation parameters are summarized in Table 1. The FE mesh is fixed and composed of 90<sup>3</sup> isotropic tetrahedral elements. The simulation time step  $\Delta t$  is set to 5 s.

The same simulation has also been performed without any coloring, which corresponds to the initial formalism detailed in Section 2, in order to illustrate the gains in efficiency permitted by the new implementation. As illustrated in Fig. 10, the number of needed GLS functions remains much lower all along the simulation with the  $C_2$  criterion, which is thus proven more efficient than  $C_1$  for microstructures presenting strong grain size heterogeneities. Obviously, without coloring algorithm the number of distance fields is equal to the number of grains.

Simulations are performed on 6 Intel Xeon CPUs. Table 2 provides the computation times and their distributions. The average number of active distance fields during a simulation is noted  $\langle N_p \rangle$ . It is equal to 343 without coloring and falls down to 21 with the previous optimizations, which results in a great improvement of the simulation time.

Next, the optimized simulation using the coloring algorithm coupled with the  $C_2$  swapping criterion is defined as reference configuration. The computation time and the average number of needed GLS corresponding to this simulation are noted,  $t_s^{C_2}$  and  $\langle N_p \rangle^{C_2}$ , respectively, and Table 2 provides  $t_s^{C_2} = 1$  h08 min and  $\langle N_p \rangle^{C_2} = 21$ . Based on the results of Table 2, a simple linear relationship with slope 0.5 can be obtained between the number of active GLS functions  $\langle N_p \rangle$  and the simulation time  $t_s$ :

$$\frac{t_s - t_s^{C_2}}{t_s^{C_2}} = 0.5 \frac{\langle N_p \rangle - \langle N_p \rangle^{C_2}}{\langle N_p \rangle^{C_2}}. \quad (15)$$

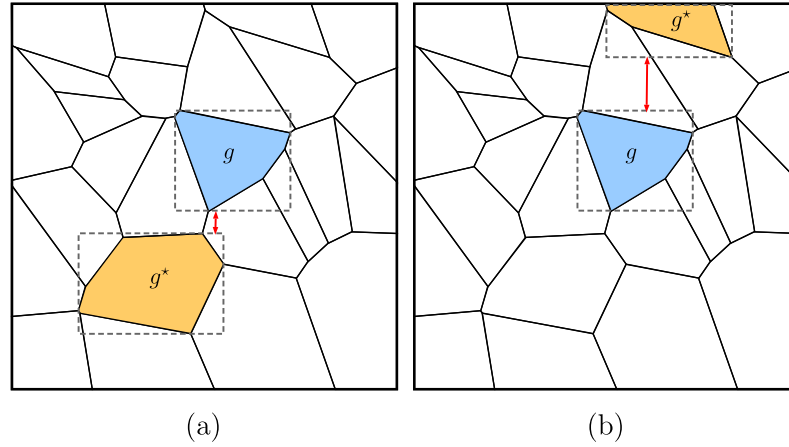


**Fig. 9.** Calculation of the distance between the bounding boxes of  $g$  and  $g^*$  (represented by the red thick arrow) and decision concerning  $g^*$ : (a)  $g^*$  must be included in  $\mathcal{L}(g)$ ; (b)  $g^*$  can be safely ignored. (For interpretation of the references to color in this figure legend, the reader is referred to the web version of this article.)

**Table 1**

Input parameters for the simulation of a 5 min heat treatment using the polycrystal of Fig. 8(b).

| Parameter  | Value               | Units                                    |
|------------|---------------------|--|
| $T$        | 1000                | °C                                       |
| $\Delta t$ | 5                   | s  |
| $M$        | $5 \times 10^{-13}$ | $\text{m}^4 \text{J}^{-1} \text{s}^{-1}$ |
| $\gamma$   | 0.6                 | $\text{J m}^{-2}$                        |
| $r$        | 11                  | $\mu\text{m}$                            |
| $e_0$      | 0                   | $\text{J m}^{-3}$                        |

**Table 2**

Distribution of the computation time for the simulation of a 5 min heat treatment at 1000 °C using the polycrystal of Fig. 8. Simulations are performed on 6 Intel Xeon CPUs.

|                               | Without coloring | $C_1$ criterion | $C_2$ criterion |
|-------------------------------|------------------|-----------------|-----------------|
| $\langle N_p \rangle$         | 343              | 90              | 21              |
| Solving of CDEs (see Eq. (5)) | 7 h09 min        | 1 h56 min       | 27 min          |
| Reinitialization              | 2 h01 min        | 1 h02 min       | 38 min          |
| Others                        | 37 min           | 8 min           | 3 min           |
| Total simulation time         | 9 h47 min        | 3 h06 min       | 1 h08 min       |

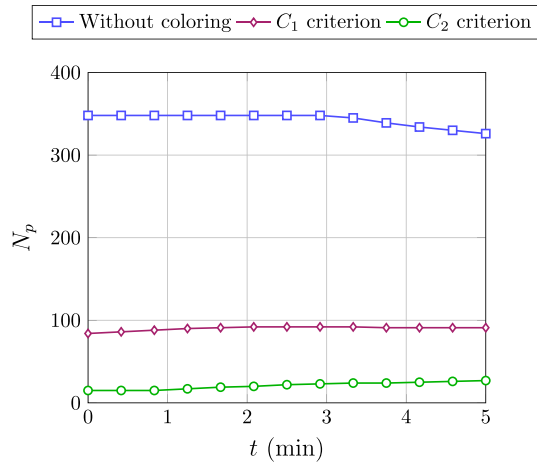


**Fig. 10.** Number of active GLS functions during the simulation of a 5 min heat treatment at 1000 °C using the initial polycrystal of Fig. 8.

It undermines that the computation time is not proportional to the number of distance fields. This finding may seem surprising but can be actually easily explained by analyzing the execution time of the reinitialization algorithm (see Table 2). For each distance field, a piece-wise representation of the interface is firstly constructed at the early stage of the reinitialization algorithm. The complexity of a distance computation is, on average, a logarithmic function of the number of elements constituting this discretized contour [3]. As fewer distance fields are employed in the new formalism, each contains more grains, which increases the interface length and therefore the number of facets. Consequently the reinitialization of a distance field taken separately requires more efforts when coloring is employed, which justifies that the cost of this operation is

not a linear function of the number of GLS functions. The global computation time devoted to reinitialization is however reduced by a factor up to 3 thanks to the new implementation, which is still very interesting.

#### 4. 3D simulation of SRX using results of CPFEM computations

In this section, we investigate the deformation of a 3D polycrystal with subsequent SRX in site-saturated conditions. A RVE is firstly submitted to a channel-die compression test and its mechanical state after deformation is used as input to perform several SRX simulations. Different configurations are investigated in which site-saturated and bulk nucleation are considered with either heterogeneous or homogeneous stored energy distribution. The model predictions are confronted with the experimental work of Huang [24], wherein a 304L material has been submitted to hot torsion tests with subsequent heat treatment in various thermo-mechanical conditions, in order to investigate DRX, PDRX or SRX.

##### 4.1. Deformation of the polycrystal

The behavior of the aggregate during the deformation is described by a CPFEM model, based on a classical elastoviscoplastic formulation. This model assumes that elastic strains are infinitesimal and plastic deformation is achieved by dislocation slip along the  $\{111\}\langle 110 \rangle$  crystallographic system, expected in FCC crystals deforming at low temperature. The details and validation of the constitutive time integration scheme can be found in [25,15]. A viscoplastic exponential flow-rule is used to relate the slip rates to the applied stress [26]:

$$\dot{\gamma}^{\alpha} = \dot{\gamma}_0 \left| \frac{\tau^{\alpha}}{\tau_c} \right|^{1/m} \text{sign}(\tau^{\alpha}), \quad (16)$$

by considering for each slip system  $\alpha$ ,  $\dot{\gamma}^\alpha$  which is the rate of dislocation slip and  $\tau^\alpha$  which is the resolved shear stress. The coefficient  $\dot{\gamma}_0$  is a reference slip rate,  $m$  is the sensitivity exponent and  $\tau_c$  is the critical resolved shear stress which is assumed to be identical for all slip systems [16]. This model also considers two populations of dislocations:

- the statistically stored dislocations (SSDs) which are the dislocations accumulated in the material during homogeneous plastic deformation,
- the geometrically needed dislocations (GNDs) which appear in areas of strain gradient and thus ensure the crystal lattice continuity.

The total dislocation density inside the material, noted  $\rho$ , is naturally the sum of the densities corresponding to these two populations. The critical resolved shear stress evolves with the dislocation density according to the following hardening law:

$$\tau_c = \tau_0 + \frac{1}{2} \mu b \sqrt{\rho}, \quad (17)$$

where  $b$  and  $\mu$  correspond respectively to the norm of the Burgers vector and the elastic shear modulus of the material.

We refer the interested reader to [25,15,16,22] for further details concerning the temporal evolution of the dislocation densities, the CPFEM model and the FE formulation.

A polycrystal composed of 100 grains with initial dimensions  $0.62 \times 0.62 \times 0.62 \text{ mm}^3$  is submitted to a planar compression test and deformed until the averaged strain inside the material reaches a value of 30%. The FE mesh is composed of  $100^3$  unstructured tetrahedra and remeshing operations are performed every 5% of deformation in order to ensure a good overall element quality all along the simulation. At the end of the deformation, the energy field  $\mathcal{D}$  is deduced from the dislocation density field according to:

$$\mathcal{D}(x) = \frac{1}{2} \mu b^2 \rho(x), \quad (18)$$

The final FE mesh and the GLS functions are then used as input for the SRX simulations. Considering the initialization of the energy fields  $\mathcal{E}_k$ , two different distributions are investigated. In the former, the average value of the field  $\mathcal{D}$  is affected to all the grains of the polycrystal, which results in a homogeneous distribution of the stored energy. This first simplified configuration permits comparisons with the Johnson–Mehl–Avrami–Kolmogorov (JMAK) theory, which assumes a homogenized deformation energy throughout the microstructure. Hereafter the term “Homogeneized Energy” designates this configuration.

In the second distribution, the energy of a given grain with index  $g$  belonging to the  $i^{\text{th}}$  GLS function is calculated by averaging the values of  $\mathcal{D}$  on the set of nodes located inside this grain  $\mathcal{N}_{g,i}$ . In this configuration, the function GENERATE\_ENERGY() of Algorithm 1 can be described by Algorithm 3. Obviously this representation, referred as “Heterogeneous Energy”, is much more realistic

because it also considers energy gradients between deformed grains.

**Algorithm 3.** Generation of the grain energy in the “Heterogeneous Energy” representation

---

```

procedure GENERATE_ENERGY Field  $\mathcal{I}_i$ , Field  $\mathcal{D}$ , Integer  $g$ 
  Create Floats  $e \leftarrow 0$  and  $o \leftarrow 0$ 
  for Node  $n \in \mathcal{M}$  do
    if  $\mathcal{I}_i(n) == g$  then
       $e \leftarrow e + \mathcal{D}(n)$ 
       $o \leftarrow o + 1$ 
    end if
  end for
  Process synchronization  $\rightarrow$  sum the values obtained by each
  process for  $e$  and  $o$ 
  return  $e/o$ 
end procedure

```

---

The dislocation density in the annealed material is around  $10^{11} \text{ m}^{-2}$  and is more than three thousand times smaller than the ones resulting from the CPFEM simulation. It can thus be reasonably neglected. As a consequence nuclei receive initially a null energy (i.e.  $e_0 = 0$ ).

In the present study, the energy is considered homogeneous for a given grain, which remains a strong assumption. In real materials, intragranular heterogeneities may result in different migration rates for the grain boundaries. Ongoing studies attempt to address this limitation by considering heterogeneous stored energy fields inside the grains [27]. Furthermore, we assume here that the grain energies do not evolve during the treatment, which can also be improved. Thus in our framework, when a migrating grain boundary sweeps into the interior of a neighbor grain, the energy of this advancing grain is naturally affected inside the migration region, which remains a strong hypothesis. This approach has nevertheless the advantage of avoiding a specific treatment in the migration zone. On the other hand, updating the crystal orientation field in the context of DRX requires much more attention and a specific approach has then been developed very recently [22]. The latter relies on an extension of the crystal orientation field, which is performed during reinitialization, as detailed in Section 3.2.

It is well known that nucleation plays an important role in the kinetics of recrystallization. In this study we consider nucleation in site-saturated conditions with different spatial distributions for the germs. In “Bulk” nucleation,  $\mathcal{P}$  contains all the nodes from the FE mesh, while it is only composed of the nodes close from the grain boundaries in the case of “Necklace-Type” nucleation. Two different approaches are also tested for the determination of the nucleation site:

- “Site of Highest Energy” in which the node  $n \in \mathcal{P}$  having the highest energy value (related to the field  $\mathcal{D}$ ) is chosen as nucleation site,
- “Random Nucleation” wherein the nucleation site is randomly picked in  $\mathcal{P}$ .

After one germ has been created, all the mesh nodes located inside ( $\phi > 0$ ) are removed from  $\mathcal{P}$ . Five configurations are thus simulated, which are summarized in Table 3.

#### 4.2. Determination of the nucleation parameters, a multiscale approach

Static recrystallization may occur when a deformed material is subsequently annealed. In [28], the critical dislocation density

**Table 3**  
Description of the simulated SRX configurations.

| Configuration | Energy distribution  | Nucleation                           |
|---------------|----------------------|--------------------------------------|
| 1             | Homogeneous energy   | Bulk/random nucleation               |
| 2             | Homogeneous energy   | Necklace-type/site of highest energy |
| 3             | Heterogeneous energy | Bulk/random nucleation               |
| 4             | Heterogeneous energy | Necklace-type/site of highest energy |
| 5             | Heterogeneous energy | Bulk/site of highest energy          |

**Table 4**  
Processing conditions and input parameters for the SRX simulations.

| Parameter        | Value                  | Units               |
|------------------|------------------------|---------------------|
| $T$              | 1000                   | °C                  |
| $\dot{\epsilon}$ | 0.01                   | $s^{-1}$            |
| $b$              | $2.54 \times 10^{-10}$ | m                   |
| $\mu$            | $4.55 \times 10^{10}$  | Pa                  |
| $M$              | $5 \times 10^{-13}$    | $m^4 J^{-1} s^{-1}$ |
| $\gamma$         | 0.6                    | $J m^{-2}$          |
| $K_1$            | $1.01 \times 10^{15}$  | $m^{-2}$            |
| $K_2$            | 3.3                    |                     |
| $\tau$           | $1.47 \times 10^{-9}$  | N                   |
| $\theta$         | 0.3                    |                     |
| $K_g$            | $7 \times 10^8$        | $m^{-2} s^{-1}$     |
| $b_g$            | 3                      |                     |
| $r$              | 11                     | $\mu m$             |
| $e_0$            | 0                      | $J m^{-3}$          |

needed to trigger SRX is identified through experimental tests. However, a large number of experiments has to be performed with different strain rates and annealing temperatures in order to correctly estimate this threshold value. Recently a mean field model of DRX [29] and its adaptation to SRX [30] have been proposed. The equations of this SRX model are used to estimate the critical dislocation density  $\rho_c$ , the number of nuclei  $\gamma$  and their initial radius  $r$ , which are needed inputs for the full field simulations (see Table 4).

It has been demonstrated in [30] that  $\rho_c$  can be estimated by solving the following equation:

$$\rho_c = \theta \left[ \frac{-2\gamma\dot{\epsilon} \frac{K_2}{M\tau^2}}{\ln\left(1 - \frac{K_2}{\theta K_1} \rho_c\right)} \right]^{1/2}, \quad (19)$$

where  $K_1$  and  $K_2$  represent, respectively, the strain hardening and the recovery terms in the Yoshie–Laasraoui–Jonas equation [31] used to compute the evolution of the SSD density. The parameter  $\theta$  is a constant whose value is close to 0.3 [24] and  $\tau$  is the dislocation line energy.

We consider that nuclei appear in areas where the dislocation density is greater than the critical value  $\rho_c$ . Consequently, in the mean field theory nucleation only happens in grains whose the homogenized dislocation density is greater than  $\rho_c$ . As the nucleation rate is difficult to evaluate experimentally, it is assumed that only a certain percentage of the potential nucleation sites actually nucleates. According to [29], the number of germs created in each representative grain with index  $i$  and radius  $R_i$ , noted  $\gamma_i$  is obtained by solving:

$$\gamma_i = K_g(T, \dot{\epsilon}) S_c \frac{N_i R_i^q (\rho_i - \rho_c)^{b_g}}{\sum_{\rho_k > \rho_c} N_k R_k^q (\rho_k - \rho_c)^{b_g}}, \quad (20)$$

where  $b_g$  is a constant which should be close to 3, according to Montheillet et al. [32],  $K_g$  is a probability constant depending on the processing conditions and  $S_c$  is the total surface area of the grains whose dislocation density is greater than  $\rho_c$ . The exponent  $q$  is equal to 2 or 3, depending whether it is assumed necklace or bulk nucleation. [29]. As the full field model provides a complete description of the polycrystal, all the intrinsic characteristics (equivalent radius, dislocation density, surface area) of the grains can be directly calculated without approximation. As a consequence, each of them can be considered as a representative grain in the mean field description, giving  $N_i = N_k = 1 \forall i, k$  in Eq. (21). Finally, the total number of nuclei  $\gamma$  is obtained by summing the contributions of all the (representative) grains  $i$ :

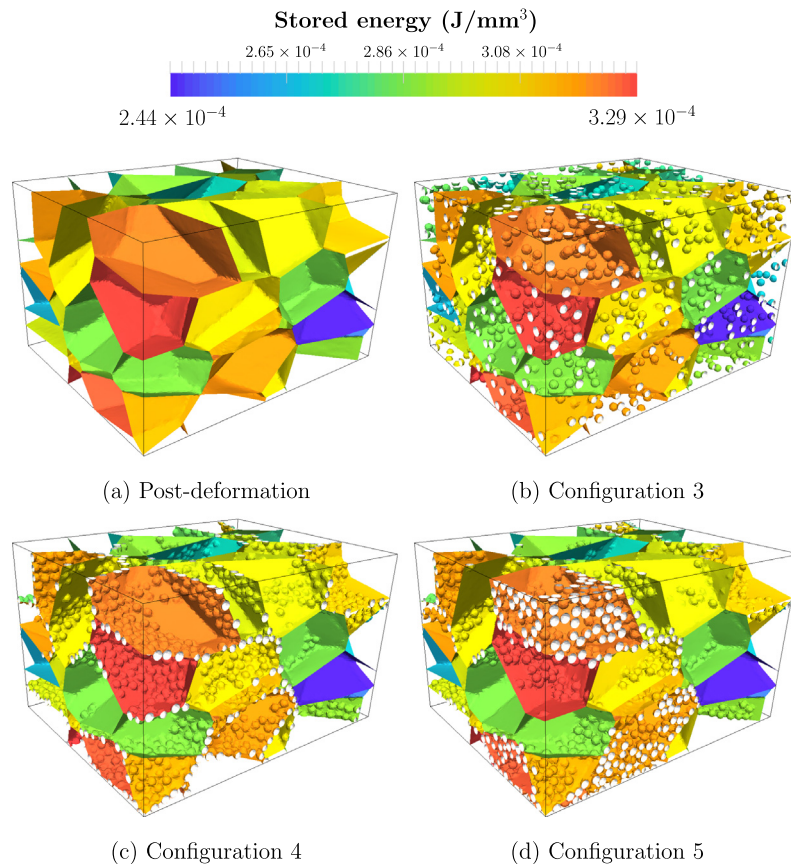


**Fig. 11.** Initial microstructure before (a) and after (b-c-d) nucleation with the “Heterogeneous Energy” representation. The color code corresponds to the stored energy. Recrystallized regions are represented in white. (For interpretation of the references to color in this figure legend, the reader is referred to the web version of this article.)

$$\mathcal{r} = \sum_i \mathcal{r}_i. \quad (21)$$

Due to the competition between the capillarity effects and energy gradients, the initial germ size must be chosen high enough to ensure their viability. The critical nuclei radius from which a germ is considered as viable is noted  $r_c$ , and the stability criterion is naturally  $r > r_c$ , with  $r$  the initial nucleus radius. In [33], the following expression is proposed to estimate this quantity:

$$r_c = \frac{4\gamma}{\langle \rho \rangle \mu b^2 + \frac{4\gamma}{\langle R \rangle}}. \quad (22)$$

The mean dislocation density at the beginning of the SRX is  $\langle \rho \rangle = 2.01 \times 10^{14} \text{ m}^{-2}$ . By using the data of Table 4 representative of the 304L steel in the considered processing conditions, Eqs. (19), (21) and (22) provide respectively  $\rho_c = 5.7 \times 10^{13} \text{ m}^{-2}$ ,  $\mathcal{r} = 3224$  for  $q = 2$  (necklace nucleation),  $\mathcal{r} = 3235$  for  $q = 3$  (bulk nucleation) and  $r_c = 3.89 \mu\text{m}$ .

Fig. 11 illustrates the initial microstructure before and after the nucleation stage for different configurations (see Table 3). It is worth emphasizing that, thanks to the new ReX formalism detailed in the previous section, each grain of the microstructure (deformed grain or nucleus) has its own energy, represented by a given color in Fig. 11. This energy is also completely independent of the GLS functions.

#### 4.3. Large scale SRX simulations

The dimensions of the REV after deformation are  $0.8 \times 0.62 \times 0.48 \text{ mm}^3$ . A refined FE mesh of  $200^3$  unstructured tetrahedra is employed for the SRX simulations in order to represent accurately the nuclei in the initial microstructure. A heat treatment of 20 min at  $1000^\circ \text{C}$  is finally simulated. The time step is set to 5 s.

The bulk recrystallized fraction, defined as the ratio between the volume of recrystallized material over the total volume, is noted  $X_v$ . The JMAK relationship is commonly used to describe its evolution during the heat treatment:

$$X_v = 1 - \exp(-Bt^n), \quad (23)$$

where  $B$  is a constant and  $n$  is the Avrami exponent. In site saturated conditions, values of 2 and 3 are expected when considering necklace and bulk nucleation, respectively. As the JMAK theory assumes a homogeneous deformation energy throughout the microstructure, only configurations 1 and 2 are considered for this first comparison. Fig. 12 illustrates that the present full field

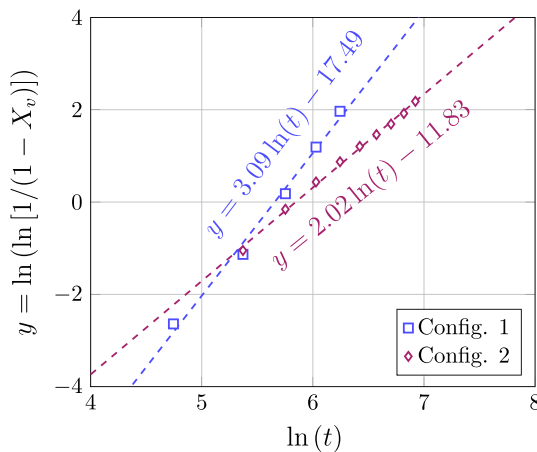


Fig. 12. Calculation of the Avrami exponent  $n$  for configurations 1 and 2 (see Table 3).

model captures greatly the recrystallization kinetics, as the calculated Avrami exponents fall very close from the expected values.

These numerical results are finally confronted with the experimental observations of [24]. Fig. 13(a) depicts the evolution of the bulk recrystallized fraction during the heat treatment for configurations 3, 4 and 5 (see Table 3).

The graph of Fig. 13(a) illustrates that configuration 4 (necklace-type nucleation with selection of the highest energy node) provides the most realistic prediction in terms of recrystallized fraction. These results are in agreement with the experimental observations of Huang [24], where nuclei appeared mainly at the grain boundaries during the recrystallization of the considered 304L steel. With bulk nucleation, the recrystallization kinetics is accelerated due to the fact that nuclei have more space to grow, because they do not interfere with each other in the initial microstructure. In configuration 5, the advance of the recrystallized front is slowed down, due to the formation of clusters in the regions of highest energy.

In [24], the recrystallization fraction is measured on slices of the material. One great advantage of the present numerical model lies on the possibility to easily interpolate the 3D fields ( $\psi_i$  and  $\varepsilon_i$ ,  $\forall i \in \{1, \dots, N_p\}$ ) on a planar mesh in order to construct a 2D representation of the microstructure from the volume results (see Fig. 14). Thus, 10 equally-spaced cutting planes of the virtual polycrystal are analyzed. We compute the respective surface recrystallized fractions of these 10 slices and then the average value  $\langle X_s \rangle$ . The evolution of this quantity is plotted in Fig. 13(b) for the configuration 4 and compared with the bulk recrystallized fraction. It appears that the surface recrystallized fraction slightly overestimates the real one, despite the number of considered cutting grains is relatively important ( $>1000$ ), which tends to indicate a small space anisotropy of the recrystallized fraction. Moreover, these results also demonstrate that the recrystallized fraction may strongly varies depending on the observed cutting plane (see the error bars in Fig. 13(b)), especially if the number of observed grains in the cutting plane is not sufficient. This numerical tool could thus be wisely used to size correctly the samples used for the experimental observations (determination of the minimal number of cutting grains), in order to guarantee that the observed slice is representative of the bulk behavior of the material.

Considering the great capacities of the present model, an exciting perspective would be to challenge the numerical predictions with more sophisticated experimental characterisations in terms of volume recrystallized fraction and grain size. Although obtaining these quantities is straightforward numerically (see Fig. 15), estimating the recrystallized grain size inside the material is rather complex experimentally. Generally, the 3D grain size is estimated from the observed one by the mean of stereological considerations, which rely on assumptions. More sophisticated methods emerged recently, such as near-field high energy X-ray diffraction microscopy (NF-HEDM) [34,35] and X-ray diffraction contrast tomography [36], but *in situ* observations are still hardly used because they require complex and specific experimental facilities.

As illustrated in Table 5 for configuration 4, each 3D simulation requires around one day of computations using 24 Intel Xeon CPUs.

The extension of the energy fields detailed in Section 3.2 is performed simultaneously with reinitialization and entails an additional cost of around 1% compared with a classical reinitialization (without field extension), which is negligible.

As the nucleation algorithm and the initialization of the energy fields are only executed one time at the early stage of the simulation, they represent a very small amount of the global computation

time. In the same way, the numerical costs associated with the SCC procedure, the nucleation algorithm, the initialization and the tracking of the energy fields are negligible compared with the reinitialization and the solving of the CDEs.

On average, 34 GLS functions are active during this simulation (22 and 37 at the early and final stage of the simulation, respectively) and the average number of grains present in the microstructure is equal to 3067. By using the expression of Eq. (15), the computation time needed for such a simulation with the initial formalism of Section 2 can be estimated around 1 month and 20 days. Thus the improvements of Section 3 result in an acceleration factor up to 45, which is quite satisfying.

**Table 5**  
Distribution of the computation time for a 3D large scale SRX simulation (configuration 4). The simulation is performed on 24 Intel Xeon CPUs.

|                                    | Related section | Computation time | Percentage |
|------------------------------------|-----------------|------------------|------------|
| Solving of CDEs                    | 2, Eq. (5)      | 8 h 24 min       | 31.4%      |
| Separation of connected components | 3.1             | 2 min            | 0.1%       |
| Initialization of energy fields    | 3.1             | <1 min           | 0%         |
| Reinitialization                   | 3.2             | 17 h 21 min      | 64.9%      |
| Field extension                    | 3.2             | 10 min           | 0.6%       |
| Tracking of grain energies         | 3.3             | <1 min           | 0%         |
| Nucleation                         | 3.4             | <1 min           | 0%         |
| Post treatment operations          |                 | 57 min           | 3.5%       |

Moreover, due to the reduction of the number of needed fields, the memory requirements are also drastically reduced.

Although very promising, the present model should nevertheless be further improved in order to capture the complexity of microstructural mechanisms involved during the forming process. First of all, the influence of anisotropy in terms of grain boundary energy and mobility should be considered. More specifically, it is well known that the real 304L material contains twin boundaries, which are currently omitted in the simulations. There are recent LS studies concerning the influence of anisotropic grain boundary features in the context of 2D grain growth [19,37,38]. To our knowledge, this topic has never been investigated in 3D with stored energy for the time being. Next, the intragranular heterogeneity in terms of stored energy and its evolution during the migration of the grain boundaries should also be considered. This point is currently under study [27,22]. In the present paper, only SRX is considered, which means that recrystallization starts only after the deformation stage. First efforts to model DRX in a level set framework with deformation of the polycrystal are very recent [22]. The numerical approach employed for the modeling of DRX works around a coupling between the CPFEM and GG/ReX models, and uses the same numerical tools detailed in this paper. Further experimental investigations should also be carried out in order to verify the values of the input parameters needed for the full field simulations (number and size of the nuclei, critical dislocation density...). Finally, as nucleation models adapted to SRX conditions are relatively scarce in the literature, using the present model to develop and/or calibrate an accurate nucleation law is also an interesting prospect.

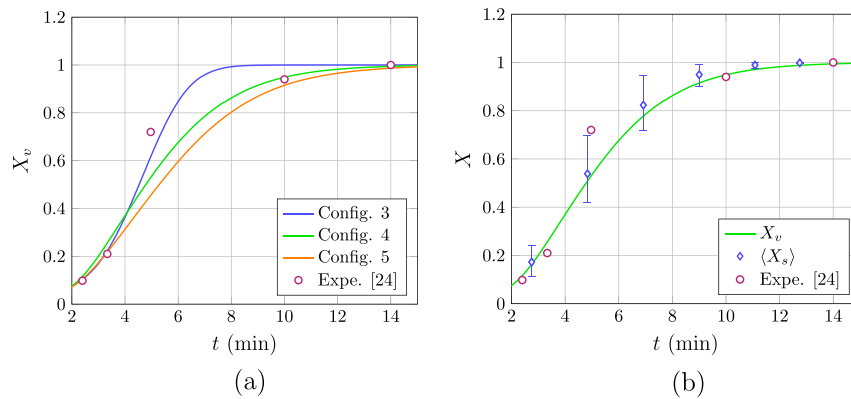


**Fig. 13.** (a) Evolution of the bulk recrystallized fraction  $X_v$  during the heat treatment at 1000 °C for the configurations 3, 4 and 5 (see Table 3), and comparison with the experimental observations of [24]; (b) comparison of the bulk and surface recrystallized fractions obtained for configuration 4. The error bars indicate the minimal and maximal values measured among the 10 slices.

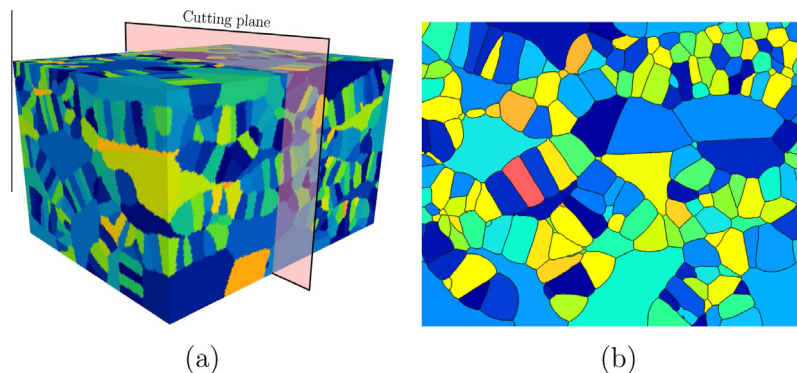


**Fig. 14.** Creation of a 2D representation of the microstructure (slice) from the 3D simulation results. The color code corresponds to the GLS functions. (For interpretation of the references to color in this figure legend, the reader is referred to the web version of this article.)



- [16] H. Resk, L. Delannay, M. Bernacki, T. Coupez, R. Logé, *Modell. Simulat. Mater. Sci. Eng.* 17 (7) (2009) 075012, <http://dx.doi.org/10.1088/0965-0393/17/7/075012>. URL <http://stacks.iop.org/0965-0393/17/i=7/a=075012?key=crossref.4fd8a48e8015bb295a60ba74e6f2351>.
- [17] H. Hallberg, *Modell. Simulat. Mater. Sci. Eng.* 21 (8) (2013) 085012, <http://dx.doi.org/10.1088/0965-0393/21/8/085012>. URL <http://stacks.iop.org/0965-0393/21/i=8/a=085012?key=crossref.fc2d86d9805f0075a83535b0524735cb>.
- [18] M. Elsey, S. Esedoglu, P. Smereka, *Phil. Mag.* 91 (2011) 1607–1642.
- [19] Y. Jin, N. Bozzolo, A. Rollett, M. Bernacki, *Comput. Mater. Sci.* 104 (15) (2015) 108–123.
- [20] M. Bernacki, R. Logé, T. Coupez, *Scripta Mater.* 64 (6) (2011) 525–528, <http://dx.doi.org/10.1016/j.scriptamat.2010.11.032>. URL <http://linkinghub.elsevier.com/retrieve/pii/S1359646210007906>.
- [21] K. Hitti, P. Laure, T. Coupez, L. Silva, M. Bernacki, *Comput. Mater. Sci.* 61 (2012) 224–238.
- [22] R. Boulais-Sinou, B. Scholtes, D. Pino Muñoz, C. Moussa, I. Poitraul, I. Bobin, A. Montouchet, M. Bernacki, Full field modeling of dynamic recrystallization in a global level set framework, application to 304L stainless steel, in: *Numiform 2016: The 12th International Conference on Numerical Methods in Industrial Forming Processes*, 2016.
- [23] F. Humphreys, M. Hatherly, *Recrystallization and Related Annealing Phenomena*, Elsevier, 2004.
- [24] K. Huang, Towards the Modelling of Recrystallization Phenomena in Multi-Pass Conditions: Application to 304L Steel, Ph.D. thesis, 2011.
- [25] L. Delannay, P. Jacques, S. Kalidindi, *Int. J. Plast.* 22 (10) (2006) 1879–1898, <http://dx.doi.org/10.1016/j.ijplas.2006.01.008>. URL <http://linkinghub.elsevier.com/retrieve/pii/S0749641906000118>.
- [26] J. Hutchinson, *Metall. Trans. A* 8 (1977) 1465–1469.
- [27] D. Ilin, B. Scholtes, N. Bozzolo, D. Pino Muñoz, M. Bernacki, Effect of intragranular strain heterogeneity on recrystallization kinetics assessed by numerical simulation at the mesoscopic scale, in: *La métallurgie, quel avenir!*, 2016.
- [28] C. Kerisit, Analyse des mécanismes de recristallisation statique du tantale déformé à froid pour une modélisation en champ moyen, Ph.D. thesis, 2012.
- [29] P. Bernard, S. Bag, K. Huang, R. Logé, *Mater. Sci. Eng.: A* 528 (24) (2011) 7357–7367, <http://dx.doi.org/10.1016/j.msea.2011.06.023>. URL <http://linkinghub.elsevier.com/retrieve/pii/S0921509311006757>.
- [30] A. Fabiano, Modelling of Crystal Plasticity and Grain Boundary Motion of 304L Steel at the Mesoscopic Scale Ph.D. thesis, Mines-ParisTech, 2013.
- [31] A. Laasraoui, J. Jonas, *Metall. Trans. A* 22 (7) (1991) 1545–1558.
- [32] F. Montheillet, O. Lurdos, G. Damamme, *Acta Mater.* 57 (5) (2009) 1602–1612, <http://dx.doi.org/10.1016/j.actamat.2008.11.044>. URL <http://linkinghub.elsevier.com/retrieve/pii/S1359645408008641>.
- [33] J. Favre, D. Fabrgue, C. Akihiko, Y. Bréchet, *Philos. Mag. Lett.* 93 (11) (2013) 631–639.
- [34] C. Hefferan, J. Lind, S. Li, U. Lienert, A. Rollett, R. Suter, *Acta Mater.* 60 (10) (2012) 4311–4318, <http://dx.doi.org/10.1016/j.actamat.2012.04.020>. URL <http://linkinghub.elsevier.com/retrieve/pii/S1359645412002765>.
- [35] R. Pokharel, J. Lind, S.F. Li, P. Kenesei, R.A. Lebensohn, R.M. Suter, A.D. Rollett, *Int. J. Plast.* 67 (2015) 217–234, <http://dx.doi.org/10.1016/j.ijplas.2014.10.013>. URL <http://linkinghub.elsevier.com/retrieve/pii/S0749641914002083>.
- [36] M. Syha, W. Rheinheimer, M. Bäurer, E. Lauridsen, W. Ludwig, D. Weygand, P. Gumbsch, *Scripta Mater.* 66 (1) (2012) 1–4, <http://dx.doi.org/10.1016/j.scriptamat.2011.08.005>. URL <http://linkinghub.elsevier.com/retrieve/pii/S1359646211004714>.
- [37] H. Hallberg, *Modell. Simulat. Mater. Sci. Eng.* 22 (8) (2014) 085005, <http://dx.doi.org/10.1088/0965-0393/22/8/085005>. URL <http://stacks.iop.org/0965-0393/22/i=8/a=085005?key=crossref.257b1290acb185e85b659f450fb18962>.
- [38] C. Mießen, M. Liesenjohann, L. Barrales-Mora, L. Shvindlerman, G. Gottstein, An advanced level set approach to grain growth – accounting for grain boundary anisotropy and finite triple junction mobility, *Acta Mater.* 99 (2015) 39–48, <http://dx.doi.org/10.1016/j.actamat.2015.07.040>. URL <http://linkinghub.elsevier.com/retrieve/pii/S135964541500511X>.